Integral solution for diffraction problems involving conducting surfaces with complex geometries. II. Application to ellipsoidal surfaces

Mohamed F. El-Hewie and Dan Fredal

Frank J. Seiler Research Laboratory, U.S. Air Force Academy, Colorado Springs, Colorado 80840-6528

The absorptivity and reflectivity are determined from the Fresnel coefficients of reflection and transmission by the complex ray-tracing method for a plane wave incident upon the surface $Z(x, y)$ of an isotropic conducting medium located in vacuum. A coordinate-dependent real refractive index of the form $\nu(Z, \sigma, \omega) = [q^2(Z, \sigma, \omega) + 2q(Z, \sigma, \omega) \cos \theta_{in} + 1]^{1/2}$ is used, where q and $\cos \theta_{in}$ are defined in part I of this series [J. Opt. Soc. Am. A 5, 200 (1988)]. Numerical results are presented for the scattered far fields, the surface waves, and the scattering and absorption efficiencies for ellipsoidal surfaces. We demonstrate the simplicity and accuracy of the complex ray-tracing method over the scalar-potentials method in solving for an absorbing medium located in parallel fields.

1. INTRODUCTION

In part I of this series[1] we generalized the expressions for q and p obtained by Stratton[2] for a plane wave incident upon a plane surface to the general case of an arbitrary surface. In the present paper we apply the theory developed in part I for ellipsoidal surfaces. Numerical results are given for a wide range of radiation wavelengths and object sizes to present quantitatively the different physical properties of the scattered fields resulting from the irradiation of an arbitrary metal surface.

The paper is divided into five sections. In Section 2 the mathematical formalism of part I is applied to ellipsoidal surfaces located in a parallel field. In Section 3 numerical results are presented for the local and integrated absorptions. In Section 4 numerical results are given for the surface currents and the scattered far fields. Our conclusions are stated in Section 5.

2. MATHEMATICAL FORMULATION

The letter I is used to denote equations from part I. Given a plane wave with a propagation constant $k = 2\pi/\lambda$ traveling in the positive z direction ($\theta_i = 0$) and using Eq. (I.10a), we get

$$q(Z, \sigma, \omega) = -(\xi\Psi - \zeta\Lambda)/k - (1 + Z_x^2 + Z_y^2)^{-1/2}. \quad (1)$$

The real part of the complex refractive index is then obtained from Eq. (I.15) by using $F_1 = F_2 = 0$ and $F_3 = 1$,

$$\nu(Z, \sigma, \omega) = (q^2 + 2q \cos\theta_{in} + 1)^{1/2}, \quad (2)$$

where, from Eq. (I.3b), $\cos \theta_{in} = (1 + Z_x^2 + Z_y^2)^{-1/2}$, and $\xi, \zeta, \Psi,$ and Λ are given by Eq. (I.8) as

$$A(Z, \sigma, \omega) = 1 - k^2 \sin^2\theta_{in}(\xi^2 - \zeta^2)/(\xi^2 + \zeta^2)^2, \quad (3a)$$

$$B(Z, \sigma, \omega) = 2k^2 \sin^2\theta_{in}\, \xi\zeta/(\xi^2 + \zeta^2)^2, \quad (3b)$$

$$\Psi(Z, \sigma, \omega) = \{0.5[(A^2 + B^2)^{1/2} + A]\}^{1/2}, \quad (3c)$$

and

$$\Lambda(Z, \sigma, \omega) = \{0.5[(A^2 + B^2)^{1/2} - A]\}^{1/2}. \quad (3d)$$

The dependence of ν, q, A, B, Ψ, and Λ on the surface coordinates Z, x, and y; the conductivity σ; and the radiation frequency ω are assumed.

An ellipsoidal surface can be represented by a coordinate function of the form

$$Z = (R^2 - \gamma^2 y^2 - x^2)^{1/2}, \quad (4)$$

where γ is the eccentricity and is given by

$\gamma = 1$ for a sphere with radius R and with its center at the origin of the Cartesian frame of coordinates

$= 0$ for an infinite cylinder of radius R with its central axis coincident with the y axis,

$0 \leqslant \gamma \leqslant 1$ for an ellipsoid with principal minor axis of $2R$, in the zx plane, and principal major axis of $2b$, on the y axis ($b = R/\gamma$).

The geometries of the three surfaces are shown in Fig. 1. To simplify notation we define the following parameters:

$$w = \gamma^2 y, \qquad g = (\gamma^2 - 1)\gamma^2, \qquad u = (R^2 + gy^2)^{1/2}. \quad (5)$$

The surface derivatives are then given by

$$Z_x = -x/Z, \quad (6a)$$

$$Z_y = -w/Z, \quad (6b)$$

and the local angle of incidence is defined by

$$\cos\theta_{in} = 1/C = Z/u, \quad (7)$$

where $C = (1 + Z_x^2 + Z_y^2)^{1/2}$ [Eq. (I.3b)]. Substituting Z_x, Z_y, and $\cos\theta_{in}$ from Eqs. (6) and (7) into Eqs. (1)–(3) gives the coordinate-dependent refractive index for the surface $Z(x, y)$. Equations (3a) and (3b) give

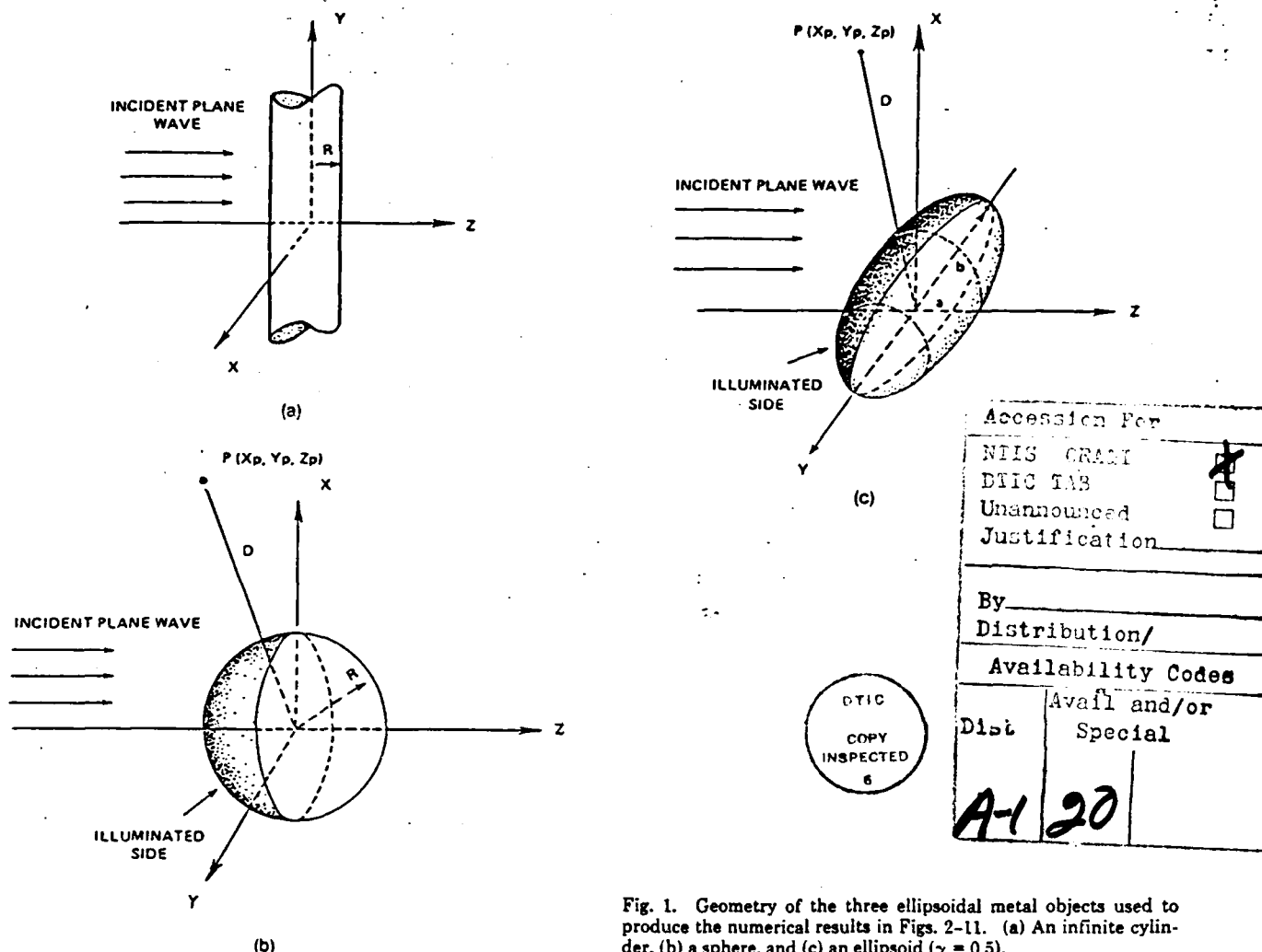M. F. El-Hewie and D. Fredal

Fig. 1.   Geometry of the three ellipsoidal metal objects used to produce the numerical results in Figs. 2–11. (a) An infinite cylinder, (b) a sphere, and (c) an ellipsoid ($\gamma = 0.5$).

$$A(Z, \sigma, \omega) = 1 - k^2[(x^2 + w^2)/u^2](\xi^2 - \zeta^2)/(\xi^2 + \zeta^2)^2 \quad (8a)$$

and

$$B(Z, \sigma, \omega) = 2k^2[(x^2 + y^2)/u^2]\xi\zeta/(\xi^2 + \zeta^2)^2. \quad (8b)$$

Ψ, Λ, q, and ν are thus determined in terms $A(Z, \sigma, \omega)$ and $B(Z, \sigma, \omega)$. In Fig. 2, numerical values for ν are plotted for aluminum, using $R = 0.1$ cm; $\gamma = 0, 0.5, 1$; and $\lambda = 0.1$ μm and $\lambda = 1.315$ μm. Figure 2(a) shows the strong coordinate dependence of ν at short wavelengths (e.g., at $\lambda = 0.1$ μm for an aluminum sphere with a radius of 0.1 cm the maximum/minimum ratio for ν is 1.0296). Figures 2(b)–2(d) show the relatively weak coordinate dependence of ν at long wavelengths (e.g., at $\lambda = 1.315$ μm the maximum/minimum ratio for ν is 1.0010 for the above-described aluminum sphere).

The Fresnel coefficients of reflection and transmission, written in terms of ν, are as follows[3]:

$$R_p = [(\nu^2 - \sin^2\theta_{in})^{1/2} - \cos\theta_{in}][\cos\theta_{in}(\nu^2 - \sin^2\theta_{in})^{1/2}$$
$$- \sin^2\theta_{in}]/[(\nu^2 - \sin^2\theta_{in})^{1/2} + \cos\theta_{in}]$$
$$\times [\cos\theta_{in}(\nu^2 - \sin^2\theta_{in})^{1/2} + \sin^2\theta_{in}], \quad (9a)$$

$$R_s = -[(\nu^2 - \sin^2\theta_{in})^{1/2} - \cos\theta_{in}]/$$
$$[(\nu^2 - \sin^2\theta_{in})^{1/2} + \cos\theta_{in}], \quad (9b)$$

$$T_p = 2\nu\cos\theta_{in}/[(\nu^2 - \sin^2\theta_{in})^{1/2}$$
$$+ \cos\theta_{in}][\cos\theta_{in}(\nu^2 - \sin^2\theta_{in})^{1/2} + \sin^2\theta_{in}], \quad (9c)$$

and

$$T_s = 2\nu\cos\theta_{in}/[(\nu^2 - \sin^2\theta_{in})^{1/2} + \cos\theta_{in}]. \quad (9d)$$

The reflectivity and the absorptivity obtained from the above coefficients are as follows:

$$\rho_p = \{[(\nu^2 - \sin^2\theta_{in})^{1/2} - \cos\theta_{in}]$$
$$\times [\cos\theta_{in}(\nu^2 - \sin^2\theta_{in})^{1/2} - \sin^2\theta_{in}]/$$
$$[(\nu^2 - \sin^2\theta_{in})^{1/2} + \cos\theta_{in}]$$
$$\times [\cos\theta_{in}(\nu^2 - \sin^2\theta_{in})^{1/2} + \sin^2\theta_{in}]\}^2, \quad (9e)$$

$$\rho_s = \{[(\nu^2 - \sin^2\theta_{in})^{1/2} - \cos\theta_{in}]/$$
$$[(\nu^2 - \sin^2\theta_{in})^{1/2} + \cos\theta_{in}]\}^2, \quad (9f)$$

$$\alpha_p = 4\nu^2 \cos\theta_{in}(\nu^2 - \sin^2\theta_{in})^{1/2}/$$

$$[(\nu^2 - \sin^2\theta_{in})^{1/2} + \cos\theta_{in}]^2$$

$$\times [\cos\theta_{in}(\nu^2 - \sin^2\theta_{in})^{1/2} + \sin^2\theta_{in}]^2, \qquad (9g)$$

and

$$\alpha_s = 4\cos\theta_{in}(\nu^2 - \sin^2\theta_{in})^{1/2}/$$

$$[(\nu^2 - \sin^2\theta_{in})^{1/2} + \cos\theta_{in}]^2. \qquad (9h)$$

Again, the dependence of the R, T, ρ, and α terms on Z, σ, and ω is assumed. The local intensity of the energy flow normal to the surface in the s wave (TE) at an arbitrary point on Z is given by Eq. (I.21) and for the p wave (TM) by Eq. (I.22). To express the local intensities in terms of the sur-

face geometry we start with Eqs. (I.17) and (I.18) and substitute $\theta_i = \varphi_i = 0$ and ϕ for the polarization angle between the electric vector on the incident fields and the x axis. This gives

$$\hat{a} = -\cos\phi\hat{i} + \sin\phi\hat{j}, \qquad (10a)$$

$$\hat{t} = (Z_y\hat{i} - Z_x\hat{j})/(Z_x^2 + Z_y^2)^{1/2}, \qquad (10b)$$

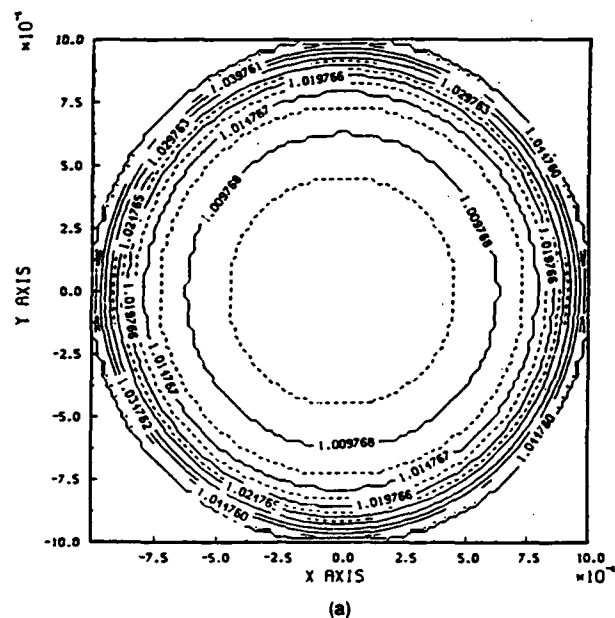$$\hat{p} = [Z_x\hat{i} + Z_y\hat{j} + (Z_x^2 + Z_y^2)\hat{k}]/[C(Z_x^2 + Z_y^2)^{1/2}], \qquad (10c)$$

$$\hat{a} \cdot \hat{t} = -(Z_x\sin\phi + Z_y\cos\phi)/(Z_x^2 + Z_y^2)^{1/2}, \qquad (10d)$$

$$\hat{a} \cdot \hat{n} = (Z_x\cos\phi - Z_y\sin\phi)/C, \qquad (10e)$$

and

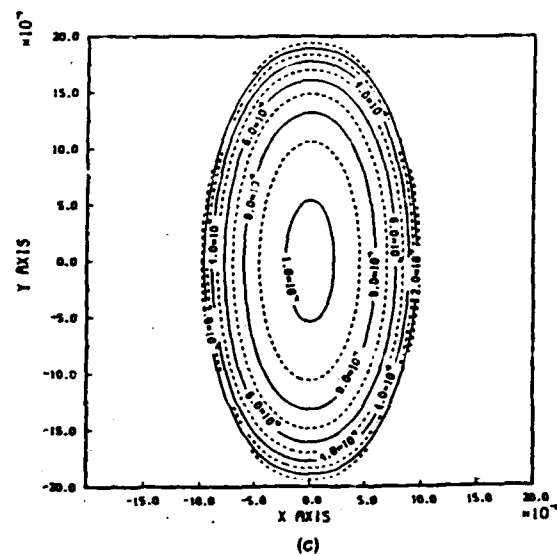$$\hat{a} \cdot \hat{p} = (-Z_x\cos\phi + Z_y\sin\phi)/[C(Z_x^2 + Z_y^2)^{1/2}]. \qquad (10f)$$

Fig. 2. Surface coordinate variation of the real refractive index ν for aluminum surfaces with $R = 0.1$ cm and $\phi = 0$. $\lambda = 0.1$ μm in (a), and $\lambda = 1.315$ μm in (b)–(d). The different object shapes used are a sphere in (a) and (c), an infinite cylinder in (b), and an ellipsoid ($\gamma = 0.5$) in (d).
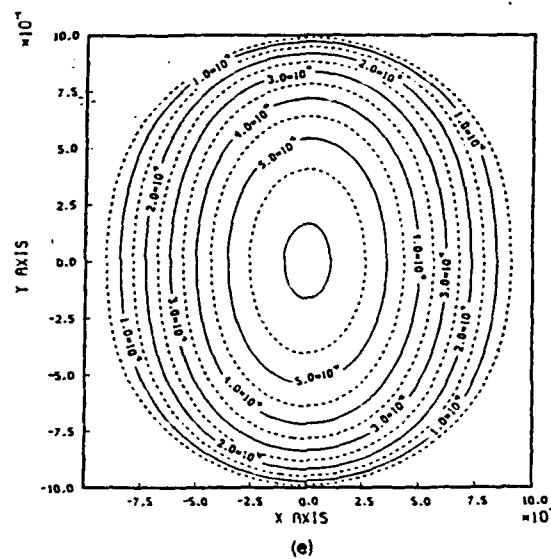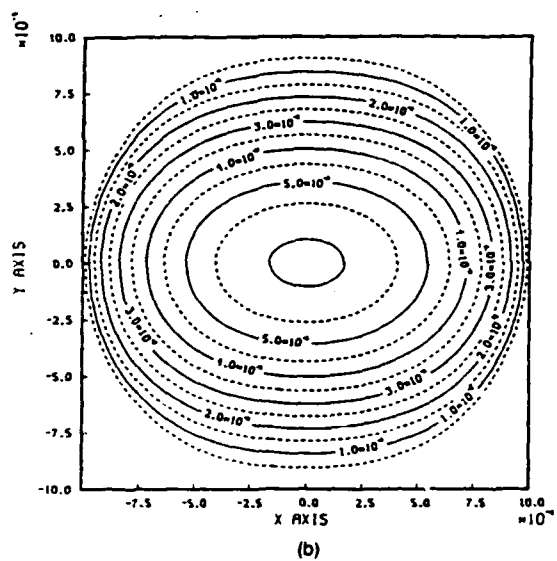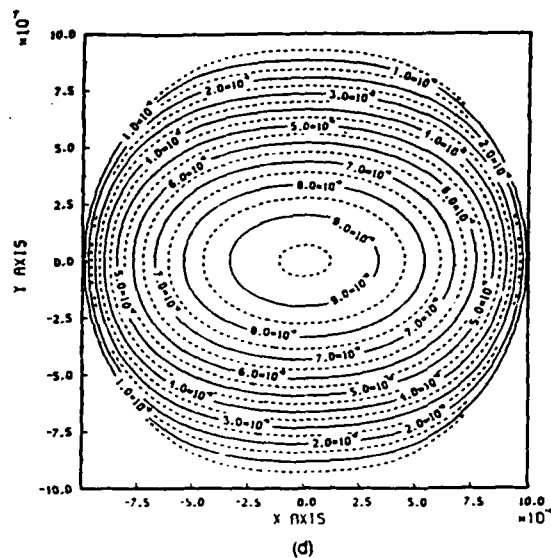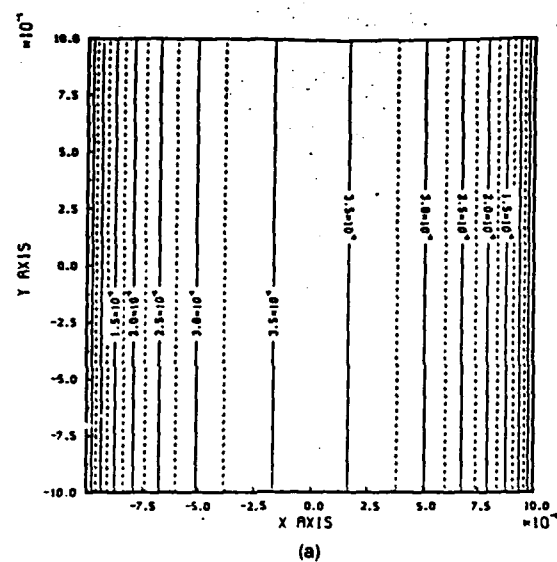
Fig. 3. Contours of equal normalized absorbed intensity at the surface of aluminum targets with $R = 0.1$ cm: $\lambda = 1.315$ μm in (a)–(c) and (e); $\lambda = 10.6$ μm in (d); $\phi = 0$ in (a)–(d); and $\phi = 90$ in (e). The different object shapes used are a cylinder in (a); a sphere in (b), (d), and (e); and an ellipsoid ($\gamma = 0.5$) in (c).
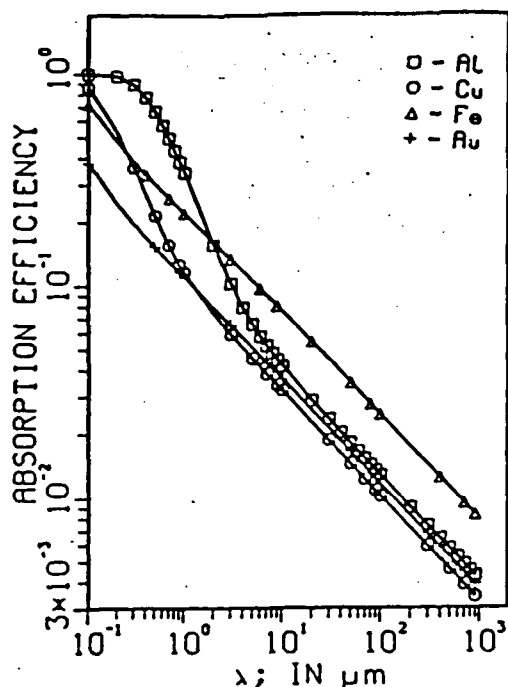
Fig. 4. Variation of the absorption efficiency with the radiation wavelength for spheres of aluminum, copper, iron, and gold, calculated by Eq. (14).

On substituting the different vector products from Eqs. (10) into Eqs. (I.21) and (I.22), we get

$$J_s^i = 0.5(E_i^2/\eta)(Z_x \sin \phi + Z_y \cos \phi)^2/[C(Z_x^2 + Z_y^2)] \quad (11a)$$

and

$$J_p^i = 0.5(E_i^2/\eta)(Z_x \cos \phi - Z_y \sin \phi)^2/[C(Z_x^2 + Z_y^2)]. \quad (11b)$$

The local currents on the surface Z are given by Eqs. (I.31) and (I.32). The various field vectors that appear in the latter two equations are obtained from Eqs. (I.19) and (10) as

$$e_s^i = -[E_i(Z_x \sin \phi + Z_y \cos \phi)/$$
$$(Z_x^2 + Z_y^2)](iZ_y - jZ_x), \quad (12a)$$

$$h_s^i = -[(E_i/\eta)(Z_x \sin \phi + Z_y \cos \phi)/$$
$$(Z_x^2 + Z_y^2)](iZ_x + jZ_y), \quad (12b)$$

$$e_p^i = -[E_i(Z_x \cos \phi - Z_y \sin \phi)/$$
$$(Z_x^2 + Z_y^2)](iZ_x + jZ_y), \quad (12c)$$

and

$$h_p^i = [(E_i/\eta)(Z_x \cos \phi - Z_y \sin \phi)/$$
$$(Z_x^2 + Z_y^2)](iZ_y^2 - jZ_x). \quad (12d)$$

Equations (8)–(12) fully determine both absorption and scattering parameters at the surface Z, as shown in Sections 3 and 4.
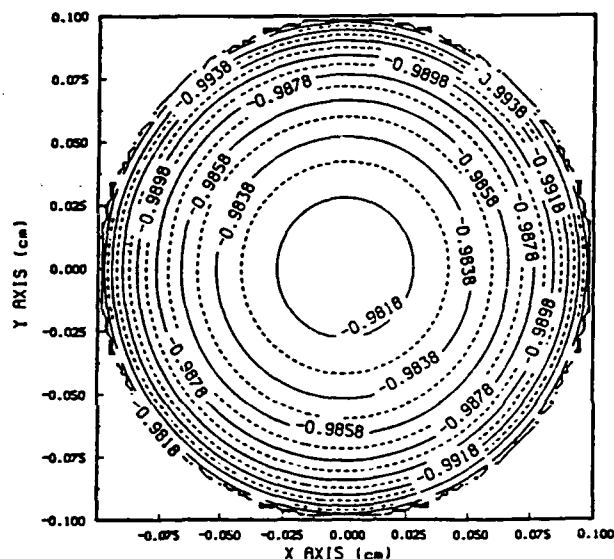
3. ABSORPTION

The total amount of power absorbed at the surface Z is obtained by integrating the local absorbed intensities over the surface area exposed to radiation,.

$$P_a = \int\int_{\Omega_a}(\alpha_p J_p^i + \alpha_s J_s^i)\cos \theta_{in}\mathrm{d}x\mathrm{d}y. \quad (13)$$
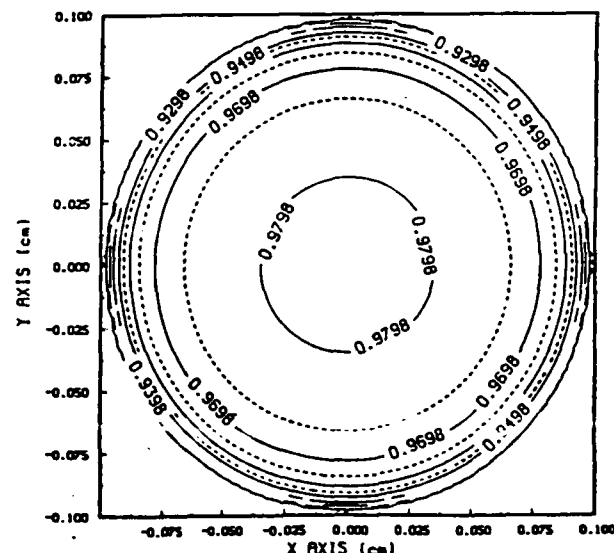
The absorption efficiency is then defined as

$$\eta_a = P_a\Big/\left(\int\int_{\Omega_a} I_i\mathrm{d}x\mathrm{d}y\right), \quad (14)$$

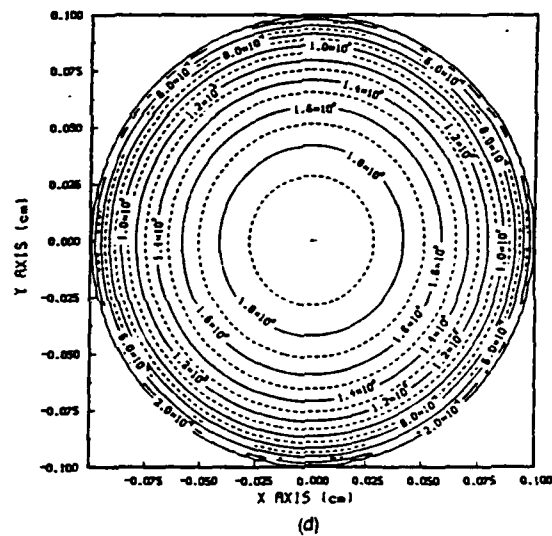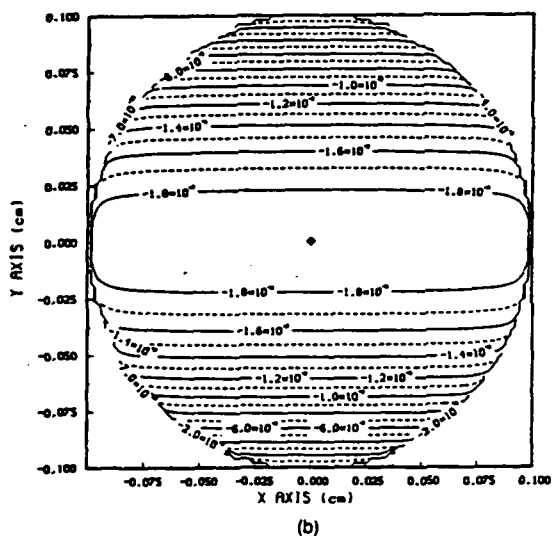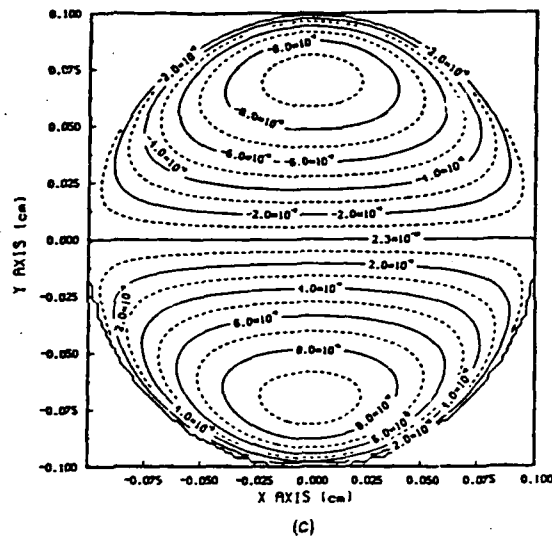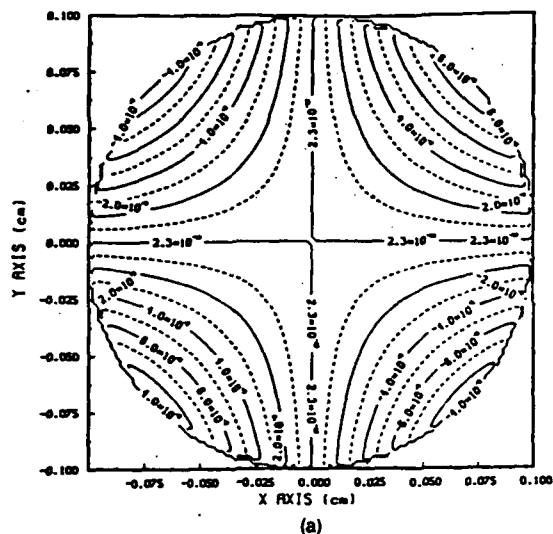where I_i is the incident intensity.

(a)

(b)

Fig. 5. Variation of the Fresnel reflection coefficients of 10.6-μm radiation at the surface of an aluminum sphere with $R = 0.1$ cm and $\phi = 0$: (a) R_s and (b) R_p.

(a)

(c)

(b)

(d)

Substituting the surface derivatives Z_x and Z_y from Eqs. (6) and the absorptivities from Eqs. (9g) and (9h) into Eqs. (11), we get

$$J_s^i = 0.5(ZE_i^2/\eta u)(x \sin \phi + w \cos \phi)^2/(x^2 + w^2) \qquad (15a)$$

and

$$J_p^i = 0.5(ZE_i^2/\eta u)(x \cos \phi - w \sin \phi)^2/(x^2 + w^2); \qquad (15b)$$

then the total absorbed power is given by

$$P_a = 0.5(E_i^2/\eta) \int\int_{\Omega_a} (Z/u)^2(x^2 + w^2)^{-1}$$

$$\times [\alpha_s(x \sin \phi + w \cos \phi)^2$$

$$+ \alpha_p(x \cos \phi - w \sin \phi)^2]dx dy. \qquad (16)$$

The area of the surface Z exposed to radiation is defined by $-1 < n_i \cdot n < 0$. Hence Ω_a is determined.

Numerical values for the local absorption [the integrand of Eq. (16)] are plotted in Fig. 3 for aluminum surfaces. The intensities are normalized by dividing by $E_i E_i^*/2\eta$, assuming that E_i is independent of the coordinates for a plane-wave incidence. In Figs. 3(a)–3(d) the electric field vector of the incident radiation is in the x direction ($\phi = 0$), which enhances the absorption along that direction. In Fig. 3(e) the electric field points in the y direction ($\phi = 90$ deg), and, as expected, the enhanced absorption is along the y direction. By examining the results from an aluminum sphere with a radius of 0.1 cm exposed to radiation of two different wavelengths [$\lambda = 1.315$ μm in Fig. 3(a) and $\lambda = 10.6$ μm in Fig. 3(d)], we note that the local absorption of the longer wavelength not only is reduced but is more dependent on polarization. This observation is based on the greater elongation of the absorption contours of the 10.6-μm radiation.

The absorption efficiency [Eq. (14)] is computed by using an automatically adaptive numerical integration method. The results are plotted in Fig. 4 for aluminum, copper, iron, and gold spheres of radius $R = 0.1$ cm. The absorption cross section Q_a is obtained by multiplying η_a by the geometrical
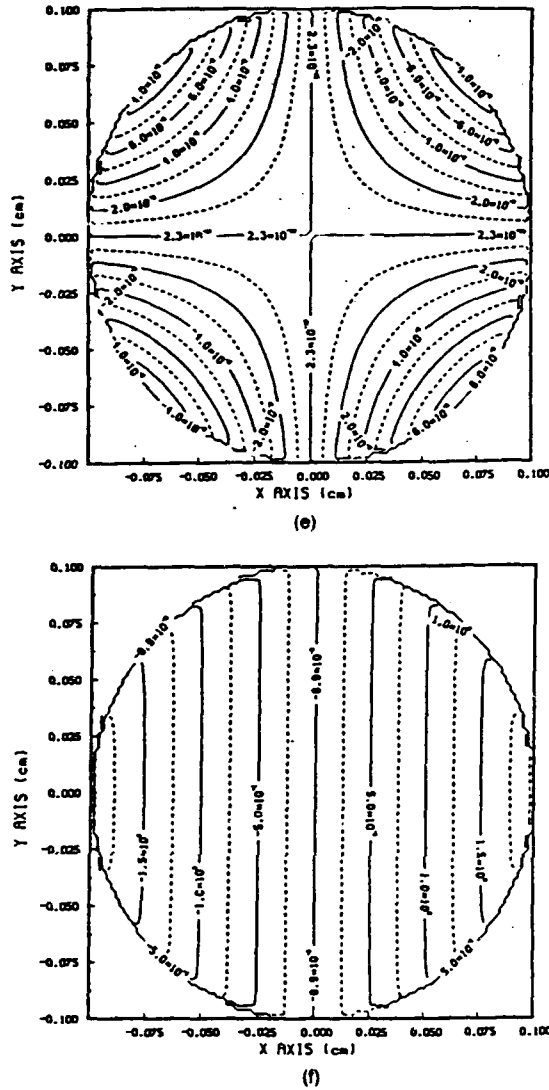
Fig. 6. Partial surface waves [Eqs. (17)] on an aluminum sphere with $R = 0.1$ cm, $\phi = 0$, and $\lambda = 10.6$ μm: (a) S_1, (b) S_2, (c) S_3, (d) T_1, (e) T_2, and (f) T_3.

cross section of the object. For a sphere of radius 0.1 cm, Q_a ranges from 0.03 cm^2 at $\lambda = 0.1$ μm to 1.25×10^{-4} cm^2 at $\lambda = 0.1$ cm. Results obtained by using the full-wave treatment and spherical harmonics (Ref. 3, Fig. 13.15) have an asymptotic value for Q_a of 0.0314 cm^2 for an iron sphere of radius 0.1 cm. This result agrees reasonably well with the Q_a obtained with our calculations. The damped oscillation (due to diffraction) of the curves of the scattering cross section versus the radiation wavelength is not accounted for in our method of solution, which is based on a complex ray-tracing approach.

4. SCATTERING

At a point $P(x_p, y_p, z_p)$ external to the surface $Z(x, y)$, the scattered field is given by Eq. (I.30). Substituting the e^i and h^i terms from Eqs. (12) into Eqs. (I.31) and (I.32) and using

$\hat{n}_b = (x_p \hat{i} + y_p \hat{j} + z_p \hat{k})/D$, where $D = (x_p^2 + y_p^2 + z_p^2)^{1/2}$, we get the following expressions for the surface currents:

$$\hat{n} \times \mathbf{e}_s = (E_i/C)(S_1 \hat{i} + S_2 \hat{j} + S_3 \hat{k}) \qquad (17a)$$

and

$$\hat{n} \times \mathbf{h}_s = (E_i/\eta C)(T_1 \hat{i} + T_2 \hat{j} + T_3 \hat{k}). \qquad (17b)$$

The S and the T terms are dimensionless parameters that account for the physical and geometrical properties of the surface, the degree of polarization, and the radiation wavelength. The S and T terms may also be defined, respectively, as the partial electric and magnetic surface waves or currents. They are obtained from Eqs. (12), (I.31), and (I.32) by

$$S_1 = [-Z_x(1 + R_s)(Z_x \sin \phi + Z_y \cos \phi)$$
$$+ Z_y(1 - R_p)(Z_x \cos \phi - Z_y \sin \phi)]/(Z_x^2 + Z_y^2), \qquad (18a)$$

$$S_2 = [-Z_y(1 + R_s)(Z_x \sin \phi + Z_y \cos \phi)$$
$$- Z_x(1 - R_p)(Z_x \cos \phi - Z_y \sin \phi)]/(Z_x^2 + Z_y^2), \qquad (18b)$$

$$S_3 = -(1 + R_s)(Z_x \sin \phi + Z_y \cos \phi), \qquad (18c)$$

$$T_1 = [Z_x(1 + R_p)(Z_x \cos \phi - Z_y \sin \phi)$$
$$+ Z_y(1 - R_s)(Z_x \sin \phi + Z_y \cos \phi)]/(Z_x^2 + Z_y^2), \qquad (18d)$$

$$T_2 = [Z_y(1 + R_p)(Z_x \cos \phi - Z_y \sin \phi)$$
$$- Z_x(1 - R_s)(Z_x \sin \phi + Z_y \cos \phi)]/(Z_x^2 + Z_y^2), \qquad (18e)$$

and

$$T_3 = (1 + R_p)(Z_x \cos \phi - Z_y \sin \phi). \qquad (18f)$$

Substituting the surface derivatives from Eqs. (6) and the surface field components of the s and p waves from Eqs. (12) into Eqs. (18), we get expressions for the S and T parameters in terms of the surface coordinates:

$$S_1 = [-(1 + R_s)(x^2 \sin \phi + xw \cos \phi)$$
$$+ (1 - R_p)(xw \cos \phi - w^2 \sin \phi)]/(x^2 + w^2), \qquad (19a)$$

$$S_2 = [-(1 + R_s)(xw \sin \phi + w^2 \cos \phi)$$
$$- (1 - R_p)(x^2 \cos \phi - xw \sin \phi)]/(x^2 + w^2), \qquad (19b)$$

$$S_3 = (1 + R_s)(x \sin \phi + w \cos \phi)/Z, \qquad (19c)$$

$$T_1 = [(1 + R_p)(x^2 \cos \phi - xw \sin \phi)$$
$$+ (1 - R_s)(xw \sin \phi + w^2 \cos \phi)]/(x^2 + w^2), \qquad (19d)$$

$$T_2 = [(1 + R_p)(xw \cos \phi - w^2 \sin \phi)$$
$$- (1 - R_s)(x^2 \sin \phi + xw \cos \phi)]/(x^2 + w^2), \qquad (19e)$$

and

$$T_3 = -(1 + R_p)(x \cos \phi - w \sin \phi)/Z. \qquad (19f)$$

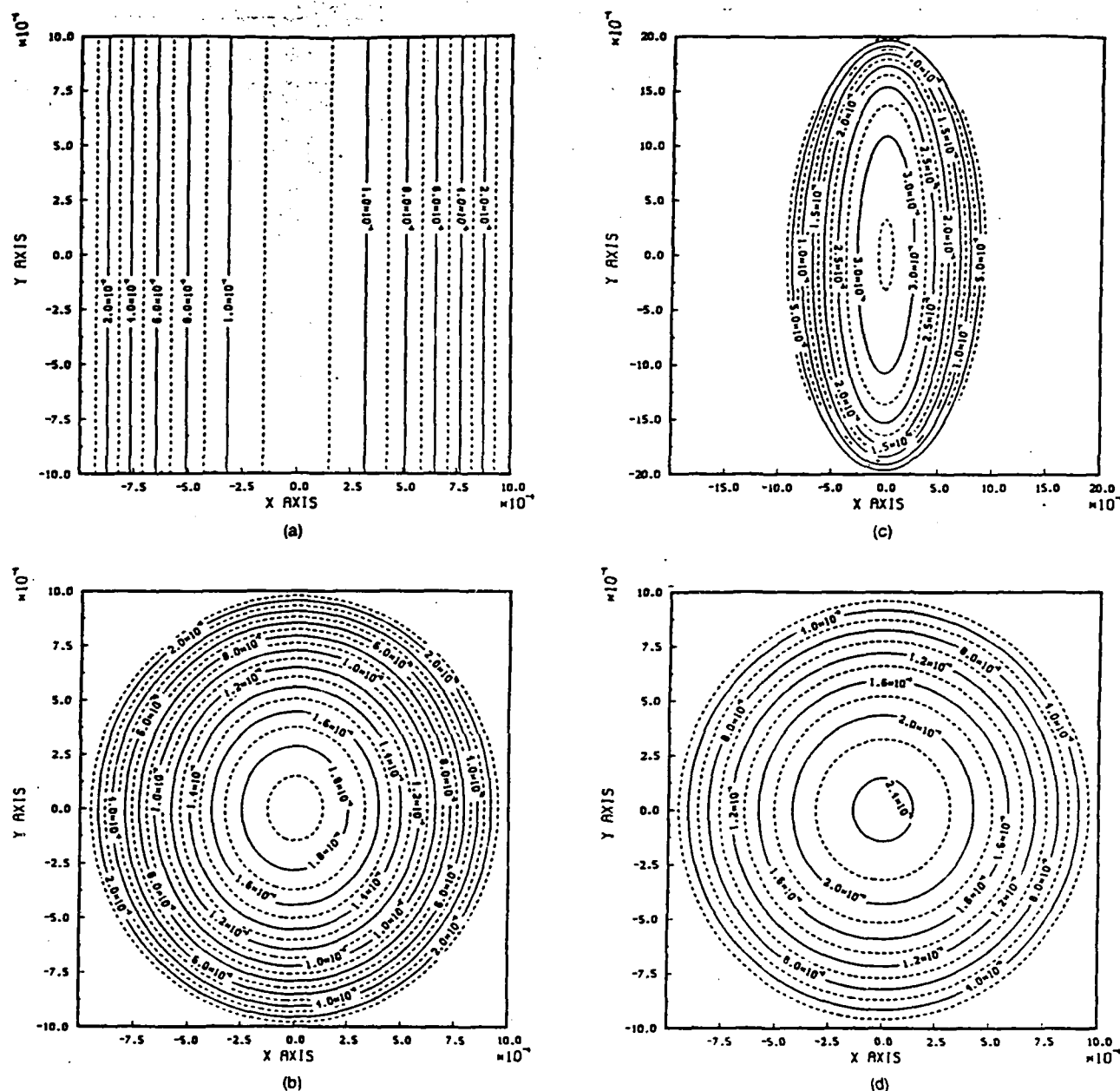It then follows that the surface currents that contribute to the scattered fields at P may be written as

M. F. El-Hewie and D. Fredal

Fig. 7.   Contours of equal scattered intensity at the surface of aluminum objects. $\phi = 0$ and $\lambda = 1.315$ μm in (a)–(c); $\lambda = 10.6$ μm in (d). The different object shapes used are a cylinder in (a); a sphere in (b) and (d); and an ellipsoid ($\gamma = 0.5$) in (c).

$$\hbar_p \times (\hbar \times e_s) = (E_i/DC)[\check{i}(y_p S_3 - z_p S_2)$$

$$+ \check{j}(z_p S_1 - x_p S_3) + \check{k}(x_p S_2 - y_p S_1)],   \quad (20a)$$

$$\hbar_p \times [\hbar_p \times (\hbar \times h_s)]$$

$$= (E_i/\eta D^2 C) \, [\check{i}[x_p z_p T_3$$

$$- (y_p{}^2 + z_p{}^2) T_1 + x_p y_p T_2]$$

$$+ \check{j} [x_p y_p T_1 - (x_p{}^2 + z_p{}^2) T_2 + y_p z_p T_3]$$

$$+ \check{k} [y_p z_p T_2 - (x_p{}^2 + y_p{}^2) T_3 + x_p z_p T_1]]. \quad (20b)$$

The three components of the scattered electric field at $P(x_p, y_p, z_p)$ are obtained by substituting the surface currents from Eqs. (20) into Eq. (I.30).   The results are

$$E_{sx}(P) = -E_i[ik \, \exp(-ikD)/4\pi D^3] \int\!\!\int_{\Omega_s} (Z/u)^2 \{(y_p S_3$$

$$- z_p S_2)D - [x_p z_p T_3 - (y_p{}^2 + z_p{}^2) T_1 + x_p y_p T_2]\}$$

$$\times \exp[ik(xx_p + yy_p + Zz_p)/D]dxdy, \qquad (21a)$$

$$E_{sy}(P) = -E_i[ik \exp(-ikD)/4\pi D^3] \int\int_{\Omega_s} (Z/u)^2\{(z_p S_1$$

$$- x_p S_3)D - [x_p y_p T_1 - (x_p^2 + z_p^2)T_2 + y_p z_p T_3]\}$$

$$\times \exp[ik(xx_p + yy_p + Zz_p)/D]dxdy, \qquad (21b)$$

and

$$E_{sz}(P) = -E_i[ik \exp(-ikD)/4\pi D^3] \int\int_{\Omega_s} (Z/u)^2\{(x_p S_2$$

$$- y_p S_1)D - [y_p z_p T_2 - (x_p^2 + y_p^2)T_3 + x_p z_p T_1]\}$$

$$\times \exp[ik(xx_p + yy_p + Zz_p)/D]dxdy. \qquad (21c)$$

Since the area of the surface Z exposed to radiation is defined by $-1 < \hat{n}_i \cdot \hat{n} < 0$ and the portion of this area that contributes to the fields at P is defined by $0 < \hat{n}_p \cdot \hat{n} < 1$, Ω_s can be determined.

The depolarization of the scattered waves is determined by defining an orthogonal system of unit vectors along the scattered rays similar to that used with the incident rays [Eqs. (10)]. Thus, if the plane of incidence of the scattered light at the point P contains the unit vectors $\hat{n}_p$ and $\hat{k}$, the orthogonal unit vectors along the scattered ray at P are

$$\hat{t}_p = \hat{n}_p \times \hat{k}/[1 - (\hat{n}_p \cdot \hat{k})^2]^{1/2} \qquad (22a)$$

and

$$\hat{d}_p = \hat{n}_p \times \hat{t}_p. \qquad (22b)$$

Substituting $\hat{n}_p = (x_p\hat{i} + y_p\hat{j} + z_p\hat{k})/D$ into the above two equations, we get

$$\hat{t}_p = (z_p\hat{j} - y_p\hat{k})/D(z_p^2 + y_p^2)^{1/2} \qquad (22c)$$

and

$$\hat{d}_p = [-(z_p^2 + y_p^2)\hat{i} + x_p y_p\hat{j} + x_p z_p\hat{k}]/D(z_p^2 + y_p^2)^{1/2}. \qquad (22d)$$

Equations (21) and (22) give the angle ϕ_p that the electric field vector makes with the plane of incidence of the scattered rays at P as

$$\cos\phi_p = \text{Re}[-(z_p^2 + y_p^2)E_{sz} + x_p y_p E_{sy} + x_p z_p E_{sz}]/$$

$$\{D(z_p^2 + y_p^2)^{1/2}[\text{Re}(E_{sz})^2$$

$$+ \text{Re}(E_{sy})^2 + \text{Re}(E_{sz})^2]^{1/2}\}. \qquad (23)$$

The scattered wave front may also be defined by surfaces of constant phase shift as obtained from Eqs. (21):

$$\Phi = \tan^{-1}[\text{Im}(E_{sz}^2 + E_{sy}^2 + E_{sz}^2)^{1/2}/$$

$$\text{Re}(E_{sz}^2 + E_{sy}^2 + E_{sz}^2)^{1/2}]. \qquad (24)$$

The above-described treatment may also be extended to the case of an aplanar light beam by taking E_i as a function in the radial coordinate. For example, for a Gaussian beam, E_i assumes the form $E_0 \exp[-(x^2 + y^2)/w_0^2]$.

The following observations of the local and far scattering can now be made:

(a)   In Fig. 5, in which the Fresnel reflection coefficients R_s and R_p [Eqs. (9a) and (9b)] are plotted, we can see that the reflection of the local p waves (TM) increases at the central parts of the surface while that of the s waves (TE) increases on the periphery.

(b)   In Fig. 6, the partial surface waves [Eq. (17)] are of the primary and the secondary orders. Partial waves of the third and higher orders, obtained by Mie (Ref. 3, Fig. 13.9), have no correspondence in the ray-tracing approach.

(c)   The normalized local fraction of the energy scattered at the surface is obtained by an equation similar to Eq. (13) but with reflectivities ρ in the place of the absorptivities α. The numerical results are plotted in Fig. 7 for three aluminum surfaces. Comparing the dependencies of the scattering contours, such as that shown in Fig. 7(a), with the absorption contours [Fig. 3(a)], we find that absorption contours are more dependent on the polarization and more elongated along the direction of polarization.

(d)   The integrated scattering efficiency, defined by an expression similar to Eq. (14) but with the scattered power in the place of the absorbed power, is plotted in Fig. 8. At wavelengths longer than 4 μm it is, to a good approximation, practical to assume that the four metals considered are infinitely conducting media with near-unity scattering efficiencies.

(e)   The scattered far-field intensity is plotted in Fig. 9. Figures 9(a)–9(c) show the scattered power from an aluminum ellipsoid illuminated by iodine laser light of a unit intensity ($\lambda = 1.315 \mu$m). At this wavelength, the maximum scattered power (as high as 70% of the incident intensity) is
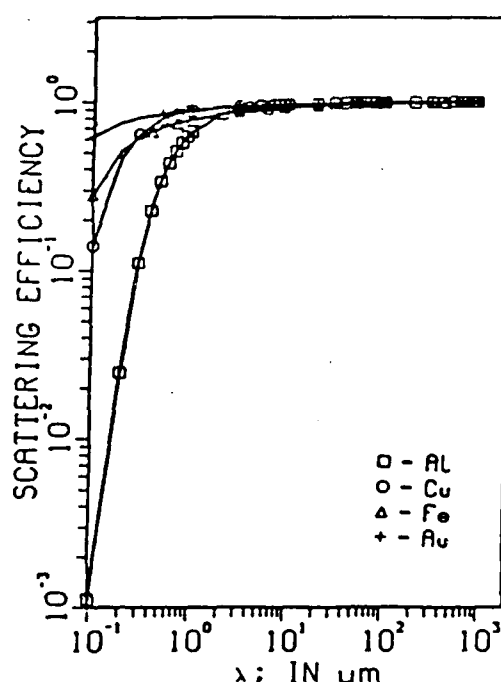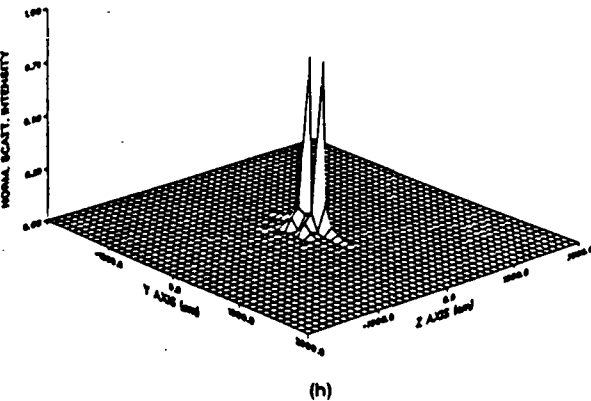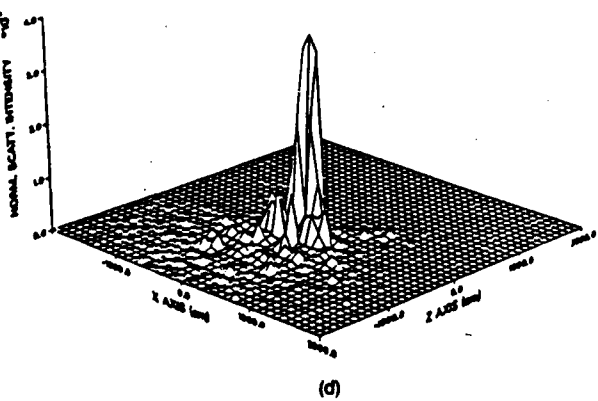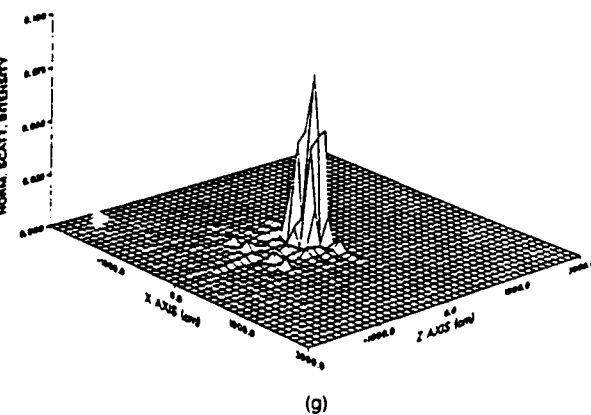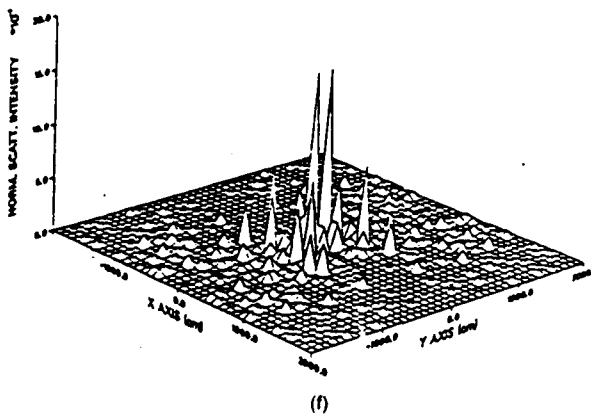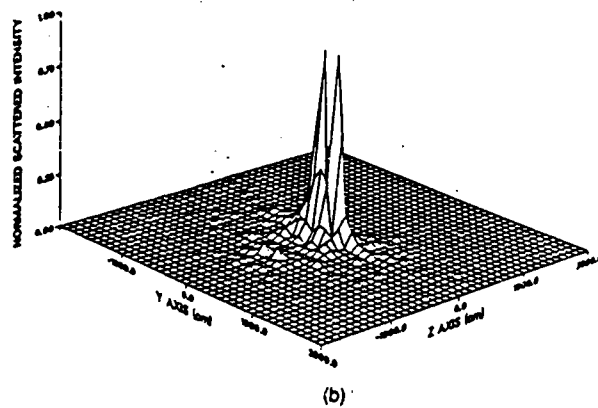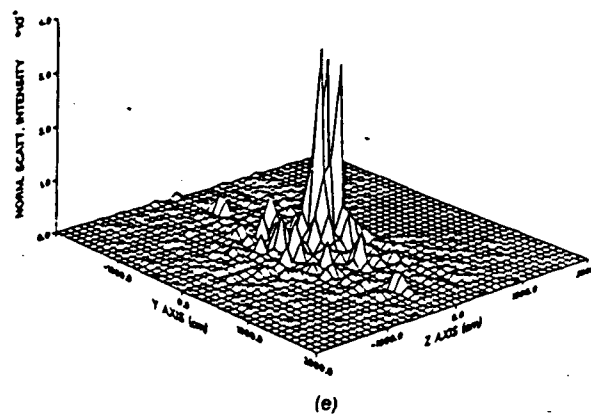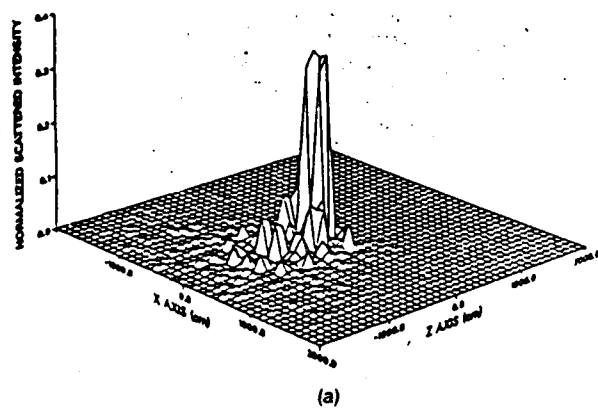

Fig. 8.   Variation of the scattering efficiency with the radiation wavelength for spheres of aluminum, copper, iron, and gold.
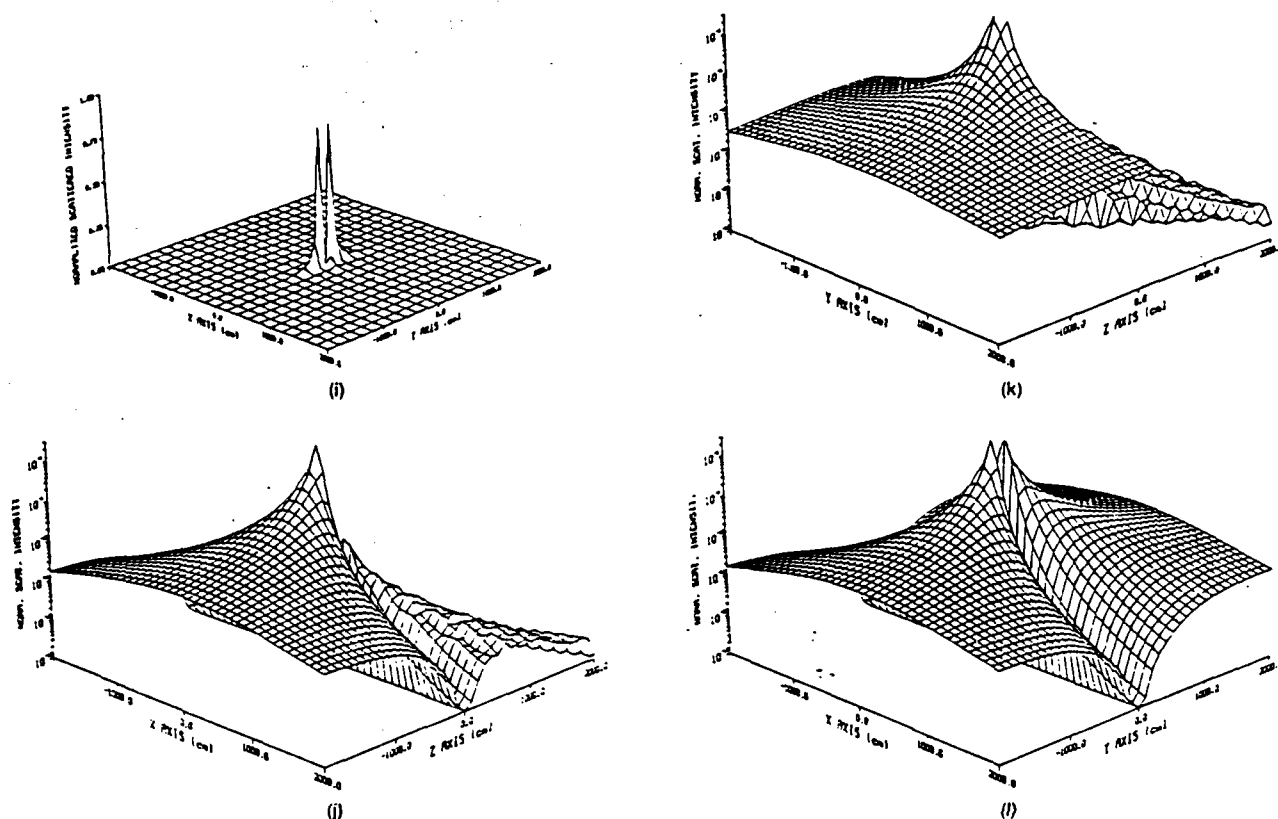
M. F. El-Hewie and D. Fredal

Fig. 9. Scattered far-field intensity from aluminum surfaces with $R = 0.1$ cm and $\phi = 0$: $\lambda = 1.315$ μm in (a)–(c) and in (g)–(i); $\lambda = 10.6$ μm in (d)–(f); $\lambda = 1$ cm in (j)–(l). The target geometries are an ellipsoid ($\gamma = 0.5$) in (a)–(f) and a sphere in (g)–(l).

contained in two sidelobes in the xy plane. Maximum back-scattering occurs at 25% in the vicinity of the surface. Figures 9(d)–9(f) represent results for CO_2 laser radiation ($\lambda = 10.6$ μm). Here, the amplitude of the scattered power is much less (maximum reflected intensity 3×10^{-3}) than for that of the iodine laser, but the side scattering perpendicular to the plane of polarization is still an important feature. Figures 9(g)–9(l) show the intensity of the far-field scattered radiation from aluminum spheres irradiated by the iodine laser [Figs. 9(g)–9(i)] and by the microwave radiation [Figs. 9(j)–9(l)].
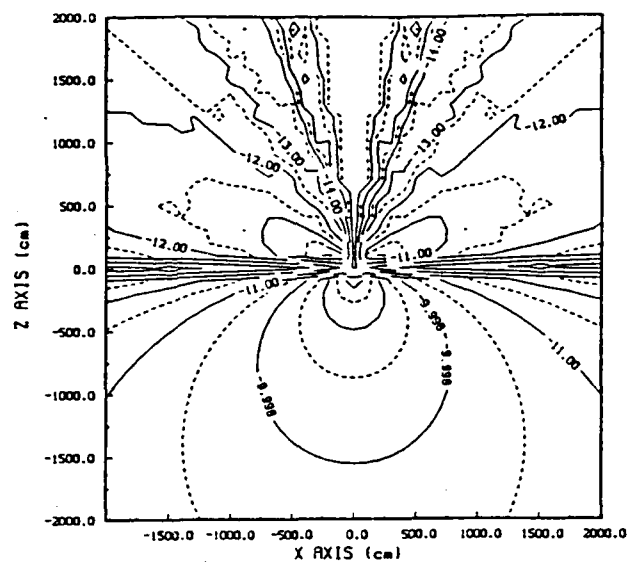
(f) Figure 10 shows contours of equal intensity of the microwave radiation scattered from aluminum spheres and is intended to demonstrate the symmetrical properties of the fields. Contours are plotted in each of the three Cartesian planes to show the symmetry of the scattered fields around $\hat{k}$, the direction of propagation; $\hat{a}$, the direction of polarization; and the surface orientation. The scattering contours are slightly distorted from circular curves in the xy plane and elliptical curves in the yz plane, and the maximum scattering intensity is as low as 10^{-8} of the incident intensity.

(g) Figure 11 is the result of rotating the plots in Figs. 9(i) and 9(k), respectively, around the x axis and the y axis to show the forward scattering patterns. The dip in the scattered power intensity in the zx plane [Fig. 11(a)] is due to the enhanced absorption in that plane (the incident electric vector points in the x direction). In Ref. 4, Fig. 8, the dip in
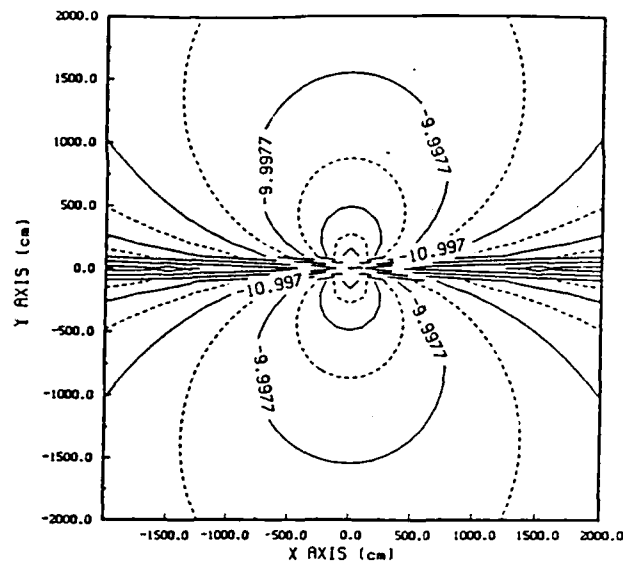
the scattered power occurred in the zy plane and was described by the diffraction effect, since the sphere used there had dimensions that were comparable with the radiation wavelength. Also, in Ref. 4, Fig. 4, with $w_0 = 4.18603\lambda$ and $R = 0.2093\lambda$, the beam spot size w_0 was taken to be large enough to cover the whole sphere, and the maximum scattered power occurred in the zy plane. The results from Ref. 4 are similar to those obtained for a plane wave, plotted in Figs. 9(c) and 9(f).
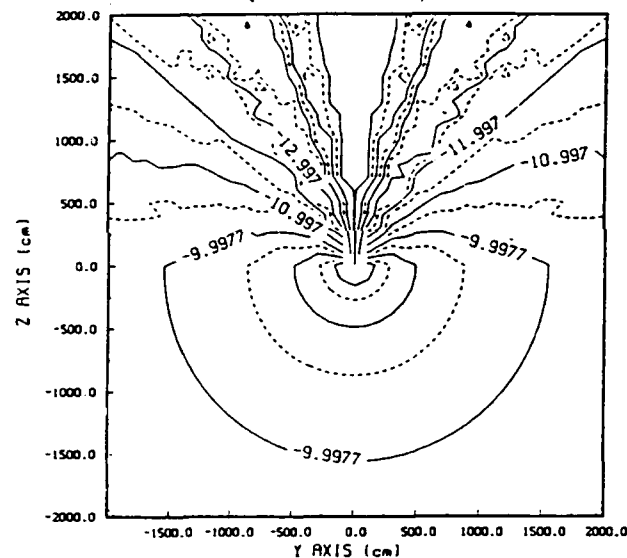
5. CONCLUSION

Based on a complex ray-tracing approach, we obtain concise analytical expressions for the far scattering fields that explicitly include the surface function $Z(x, y)$ and its physical properties, Eqs. (19) and (21). We have demonstrated the efficiency of this approach in solving for the absorption and scattering parameters of large conducting surfaces. Accurate quantitative descriptions of the magnitude, phase, and depolarization of the scattered far fields and the surface currents are presented. The results obtained are beneficial in the design of metal reflectors and in the study of the interaction of electromagnetic fields with complex conducting surfaces, as in the case of depolarization of the backscattering that is due to surface roughness. The proposed analysis can be extended easily to the case of aplanar laser beams such as Gaussian and higher-order mode beams.

M. F. El-Hewie and D. Fredal

(a)

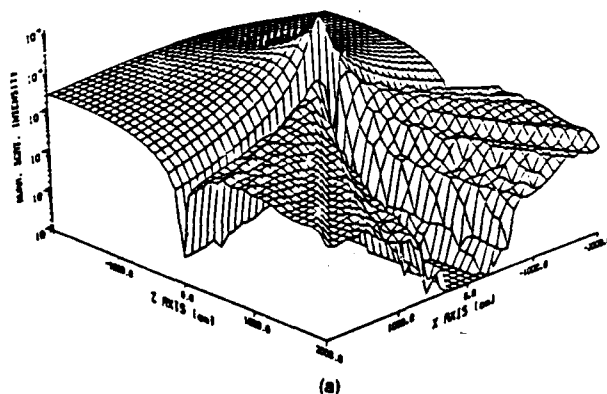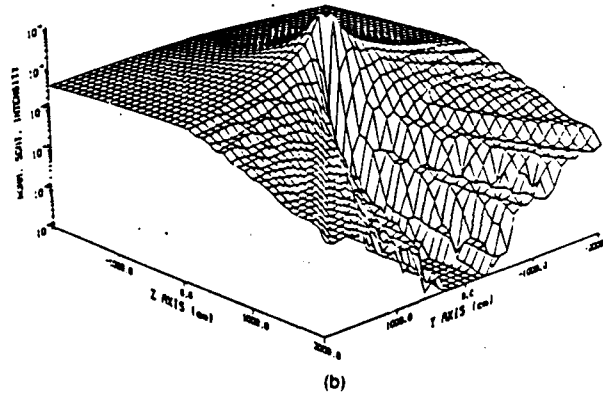(c)

(b)

Fig. 10. Contours of equal scattered far-field intensity in the three Cartesian planes from an aluminum sphere with $R = 0.1$ cm, $\phi = 0$, and $\lambda = 1$ cm. The numbers on the contours are the logarithmic values of the scattered intensities for a unit intensity of incident light. (a) xz plane; (b) yz plane; (c) xy plane.

(a)

(b)

Fig. 11. Figures 9(j) and 9(k) are rotated around the x and y axes, respectively, to show the distribution of the far-field forward scattering. (a) xz plane; (b) yz plane. $R = 0.1$ cm, $\phi = 0$, and $\lambda = 1$ cm.

ACKNOWLEDGMENT

Note added in proof: In Ref. 1, Eq. (25) should read as follows:

$$\alpha_p(Z, \sigma, \omega) = 4\nu^2 \cos\theta_{in}(\nu^2 - \sin^2\theta_{in})^{1/2}/[(\nu^2 - \sin^2\theta_{in})^{1/2}$$

$$+ \cos\theta_{in}]^2[\cos\theta_{in}(\nu^2 - \sin^2\theta_{in})^{1/2} + \sin^2\theta_{in}]^2.$$

$$(25)$$

REFERENCES

1. M. F. El-Hewie and R. J. Cook, "Integral solution for diffraction problems involving conducting surfaces with complex geometries. I. Theory," J. Opt. Soc. Am. A 5, 200–205 (1988).
2. J. A. Stratton, *Electromagnetic Theory* (McGraw-Hill, New York, 1941).
3. M. Born and E. Wolf, *Principles of Optics*, 6th ed. (Pergamon, New York, 1980).
4. W.-C. Tsai and R. J. Pogorzelski, "Eigenfunction solution of the scattering of beam radiation fields by spherical objects," J. Opt. Soc. Am. 65, 1457–1463 (1975).